atmosphere

Article

Spatiotemporal Analysis of Extreme Rainfall Frequency in the Northeast Region of Brazil

Fidel Ernesto Castro Morales [1,*], Daniele Torres Rodrigues [2,3], Thiago Valentim Marques [4], Ana Cleide Bezerra Amorim [5], Priscilla Teles de Oliveira [6], Claudio Moises Santos e Silva [3], Weber Andrade Gonçalves [3] and Paulo Sergio Lucio [3]

1 Department of Statistics, Federal University of Rio Grande do Norte, Natal, Av. Senador Salgado Filho 3000, Lagoa Nova, Natal 59078-970, Brazil
2 Department of Statistics, Federal University of Piauí, Av. Campus Universitário Ministro Petrônio Portella, Ininga, Teresina 64049-550, Brazil
3 Climate Sciences Post-Graduate Program, Department of Climate and Atmospheric Sciences, Federal University of Rio Grande do Norte, Av. Senador Salgado Filho 3000, Lagoa Nova, Natal 59078-970, Brazil
4 Federal Institute of Education, Science and Technology of Rio Grande do Norte, IFRN, Rua Brusque, 2926, Conjunto Santa Catarina, Potengi, Natal 59112-490, Brazil
5 ISI-ER—SENAI Innovation Institute for Renewable Energies, Av. Capitão Mor-Gouveia 2770, Natal 59071-355, Brazil
6 Faculdade de Ciências, Universidade Estadual Paulista, Bauru, Av. Eng. Luiz Edmundo Carrijo Coube, 14-01, Vargem Limpa, Bauru 17033-360, Brazil
* Correspondence: fidel.castro@ufrn.br

Abstract: Climate extreme events are becoming increasingly frequent worldwide, causing floods, drought, forest fires, landslides and heat or cold waves. Several studies have been developed on the assessment of trends in the occurrence of extreme events. However, most of these studies used traditional models, such as Poisson or negative binomial models. Thus, the main objective of this study is to use a space–time data counting approach in the modeling of the number of days with extreme precipitation as an alternative to the commonly used statistical methods. The study area is the Northeast Brazil region, and the analysis was carried out for the period between 1 January 1980 and 31 December 2010, by assessing the frequency of extreme precipitation represented by the R10 mm, R20 mm and R* indices.

Keywords: climatological modeling; climate change; extreme rainfall frequency; environmental data; nonhomogeneous Poisson processes; anisotropic processes

check for updates

Citation: Morales, F.E.C.; Rodrigues, D.T.; Marques, T.V.; Amorim, A.C.B.; Oliveira, P.T.d.; Silva, C.M.S.e.; Gonçalves, W.A.; Lucio, P.S. Spatiotemporal Analysis of Extreme Rainfall Frequency in the Northeast Region of Brazil. *Atmosphere* **2023**, *14*, 531. https://doi.org/10.3390/atmos14030531

Academic Editors: Flávio Justino and Roger Rodrigues Torres

Received: 25 January 2023
Revised: 22 February 2023
Accepted: 24 February 2023
Published: 9 March 2023

1. Introduction

Rainfall is one of the most important meteorological variables for climate modeling. This variable usually presents high spatial and temporal variability, which represents a great challenge when dealing with climate and meteorological phenomena. Thus, there have been several improvements in the development and application of models in recent years, such as cloud parameterization [1,2] simulations with different cumulus parameterization schemes [3–5], simulations of different climate extreme scenarios [6], modeling through probability distributions [7–9], a combination of statistical techniques for nonseasonal forecasting [10], model output statistics for seasonal rainfall forecasting [11] and multimodel seasonal forecasting as used by several prediction centers worldwide [1].

Despite advancements in the development of climate science tools, the occurrence of extreme rainfall events remains fairly difficult to predict. These events occur in all regions of the globe, and their impacts concern different sectors of society. This concern is highlighted in the assessment reports of the Intergovernmental Panel on Climate Change (IPCC). Researchers from around the globe have analyzed extreme rainfall events, whether at a global [12–14], national [15–17], regional [18–22] or local scale, such as in the cities of

Atlanta, Georgia [23], Exeter and New Hampshire in the United States [24], Stockholm in Sweden [25] and Natal in Brazil [26].

Extreme precipitation events can cause either negative or positive impacts depending on the intensity and duration of the event and on the local characteristics of the affected region. In the semiarid portion of Northeast Brazil (NEB), the occurrence of heavy rainfall events can benefit hydroelectric power generation in large watersheds [27]. In coastal NEB, on the other hand, this type of event can lead to natural disasters such as flooding and landslides [7]. Paradoxically, NEB is a region characterized by both rainfall deficits [28,29] and surpluses [19,30,31]. The rainfall distribution over this region also presents remarkable spatial and seasonal variability.

Several studies have identified that rainfall seasonality and interannual variability in NEB are directly influenced by sea surface temperature anomalies both in the Pacific and Atlantic Oceans [32–36]. However, the dynamics of extreme rainfall events regarding these anomalies are slightly different [21,37]. The El Niño and La Niña (ENSO) phenomena, for example, do not directly influence the intensity of extreme rainfall events in subregions of NEB at the annual and seasonal scales [21,38], except for a few specific cases. The effects of ENSO can be better perceived through frequency analysis, as suggested by some studies [21,38,39]. Heavy rainfall extreme event assessments at different time scales (annual, monthly and daily) have shown that these episodes can cause damage even during years considered normal or dry because most of the precipitation can occur in the course of a single month or even a few consecutive days [37]. This fact reveals the action of different meteorological systems over NEB at different temporal and spatial scales.

The studies by Min et al. [40] and Donat et al. [41] indicate an overall increase in the frequency of extreme rainfall events, which, according to Huntington [42] and Trenberth [43] are intensified by the increase in temperature. Future climate projections by the IPCC reveal an increase in mean global temperature ranging from 1.5 °C to 4.8 °C until 2100 [44]. In Brazil, an increase in temperature between 0.5 °C and 6.0 °C is expected until 2100 [45]. According to Aumann et al. [46], the projected increase of 2.7 °C in the mean temperature of tropical oceans may lead to a 60% increase in the frequency of extreme precipitation events.

In this sense, several researchers have investigated trends in the occurrence of extreme events in different regions of the globe, such as Spain [47], Portugal [48], Central Europe [49], Central Asia [50], Pakistan [51], Sub-Saharan Africa [52], Ethiopia, Kenya and Tanzania [53], Brazil [22,54–56], China [57–59] and the United States [60,61]. However, new techniques that may provide indications of the frequency of extreme rainfall events are of the uttermost importance for the development of adaptation actions for urban systems and for the reduction in risks associated with extreme climate events [26,62,63]. In this context, the main objective of this study is to use the space–time data counting approach proposed by Morales et al. [64] in the modeling of the number of days with extreme rainfall as an alternative to the commonly used statistical methods (such as Poisson and negative binomial). In particular, we investigate the frequency of extreme precipitation in NEB throughout a 31-year period from 1 January 1980 until 31 December 2010.

2. Materials and Methods

2.1. Data

The data used in this study were measured by the National Water Agency. The dataset comprises daily rainfall (mm) time series available at 151 rain gauges distributed throughout NEB (Figure 1) from 1 January 1980 to 31 December 2010. It is worth highlighting that there are less than 1.16% of gaps in the dataset, which were filled through the multiple imputation for missing data statistical technique [65], which in turn was developed by Honaker et al. [66] at the R Core Team software developer. In the present study, NEB was divided into homogeneous climate subregions as proposed by Oliveira et al. [21]: northern coast (NC), northern semiarid (NS), northwest (NO), southern semiarid (SS) and southern coast (SC). For each subregion, we analyzed extreme rainfall events through the following extreme precipitation indices [62]: R10 mm, defined as the number of days in which daily precipitation was higher than or equal to 10 mm; and R20 mm, defined as the number of days in which daily precipitation was higher than or equal to 20 mm. We also used the R^* index, which is defined as the percentage of days in which rainfall surpassed the 95% percentile for each point in the study area. In other words, for each point s in the study region, we defined:

$$R^*(s) = \sum_{t=1}^{N} 1_{(P_{95}(s),+\infty)}(y_t(s)),$$

where

$$1_{(P_{95}(s),+\infty)}(y_t) = \begin{cases} 1, \text{ if } y_t(s) > P_{95}(s) \\ 0, \text{ in any other case} \end{cases},$$

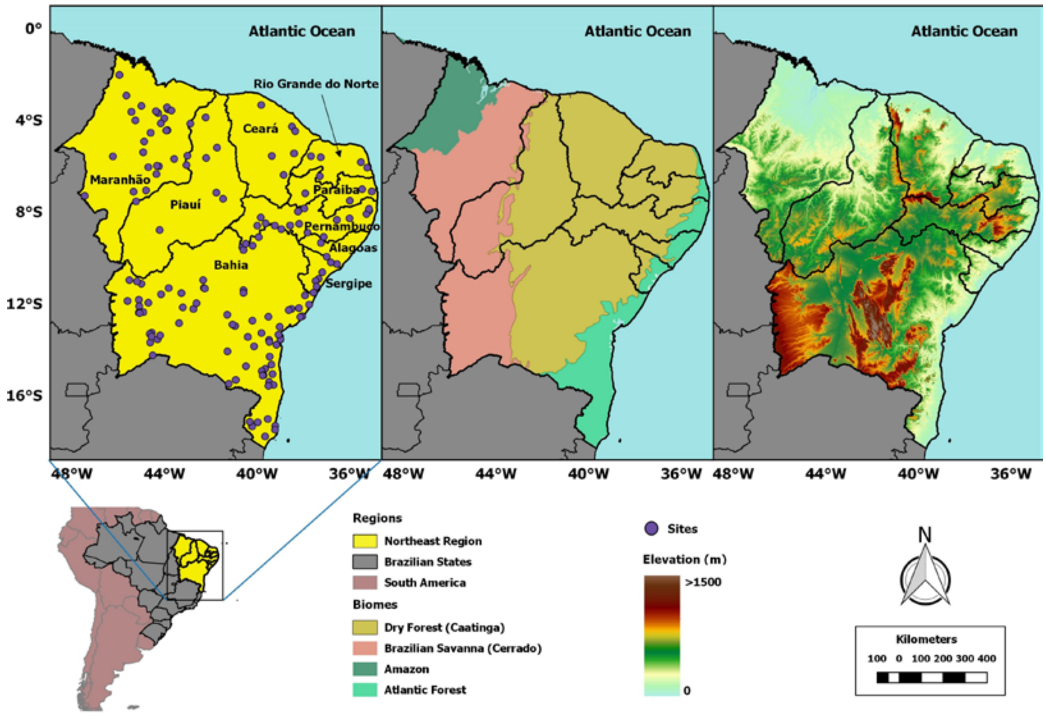

Figure 1. Location of the rain gauges (**left** panel), biome map (**center** panel) and NEB topography (**right** panel) according to the division by federal states.

N is the number of days in the year, $y_t(s)$ is the daily precipitation in the point s and $P_{95}(s)$ is the 95% percentile of observed rainfall at the $[0, T)$ time interval.

2.2. Study Area

The study area comprises NEB, located in the tropical region between coordinates 1° S and 18° S and 34.5° W and 48.5° W (Figure 1). According to the Brazilian Institute for Geography and Statistics (IBGE—Instituto Brasileiro de Geografia e Estatística), NEB has a territorial extent of 1,558,196 km^2 (18% of the total national territory) and a population of 53,078,137 (27.8% of the total Brazilian population) and encompasses nine federal units: Maranhão, Piauí, Ceará, Rio Grande do Norte, Paraíba, Pernambuco, Sergipe, Alagoas and Bahia [67]. NEB is characterized by a variety of its natural aspects (vegetation, topography, climate, etc.). It has rich biodiversity divided among four biomes: Atlantic Forest, Dry Forest (Caatinga), Brazilian Savanna (Cerrado) and the Amazon Rainforest, comprising 21%, 64%, 12% and 4% of NEB's territory, respectively, as shown in Figure 1 [67]. There is an evident topographic heterogeneity in NEB, which is characterized by a lengthy coastline and altitudes reaching up to 2033 m. The main physical features are the Borborema Plateau (higher altitudes in the Bahia and Paraíba states), the Diamantina Plateau (central portion of the Bahia state), the Mangabeiras Plateau and the Goiás Serra Geral mountain range (predominantly west of the Bahia state) [68].

Approximately 64.7% of the NEB territory is under a semiarid climate characterized by a high spatial and temporal variability in rainfall distribution [69]. NEB presents annual accumulated rainfall lower than 500 mm in semiarid regions and up to 1500 mm in coastal regions [19,70]. The SC/SS and NO/NS subregions have the maximum rainfall occurring in the summer (Dezember to February, DJF) and autumn (March to May, MAM), respectively [21]. The main atmospheric systems driving seasonal rainfall in the SC/SS subregions are the South Atlantic Convergence Zone (SACZ) [71,72] and Upper Tropospheric Cyclonic Vortices (UTCV).

The orographic characteristics of Northeast Brazil play an important role in the spatial and temporal distribution of rainfall in the region [73–76]. The presence of elevations, mountains and plateaus, as well as the proximity of the coast, can cause interference in the distribution of rainfall in the region [73], for example, this occurs in Chapada Diamantina and Serra da Borborema, which act as barriers to the passage of humid air masses, which can lead to a greater concentration of local rainfall [73,77]. In addition, the proximity to the coast may favor the formation of storms and weather systems that cause extreme rainfall in the region [77].

Palharini et al. [17] state that, in addition to other factors, extreme rainfall events can be influenced by the orographic characteristics of the region. Souza et al. [78] supported the occurrence of higher rainfall rates occurring in the highest and lowest area indices on the Sertaneja Depression. Macedo et al. [79] associated the occurrence of drought events with the cities of Araruna and Coremas, located in the NEB, the local orography. The altitude of the region can also contribute to the occurrence of natural disasters, such as the events that occurred in the city of São Gabriel in Bahia [17] and in the Cariri region of Ceará [80].

2.3. Statistical Methods

2.3.1. Model

In this paper, extreme rainfall frequency in the Northeast region of Brazil is modeled using the methods proposed by Morales et al. [64]; Morales and Vicini [81]; Morales and Rodrigues [22]. This model assumes that a nonhomogenous Poisson process of Goel [82] occurs at any point in a geographic region of interest denoted by $G,\ G \subset R^2$, in the time interval $[0,\ T)$. However, in practice, this process is observed at n fixed points (monitoring stations) in this region G, defined by $s_j = (x_j, y_j)'$, the geographic coordinate corresponding to the j-th monitoring station, $j = 1\ldots,\ n$. The mean function value m and intensity λ for this process are

$$m(s_j, t) = \theta_j\left(1 - e^{-\beta t^{\alpha}}\right), \quad (1)$$

and

$$\lambda(s_j, t) = \theta_j \beta\alpha t^{\alpha-1} e^{-\beta t^{\alpha}}.$$

where $\beta, \alpha > 0$ and $\theta_j = \theta(s_j)$ is a positive function such as $\theta_j = e^{W_j}$, where $W_j = W(s_j)$ is a random quantity that incorporates spatial dependence in the functions m and λ.

2.3.2. Spatial Component

The spatial component is incorporated through the Gaussian process $W(.)$ given by

$$W(.) \sim PG\left(\mu(.), \sigma^2(.)\rho_\phi\right),$$

where $\mu(.) = x(.)\Psi$ is the mean of the process, $x(.)$ is a covariance vector associated with the coefficient vector $\Psi,\ v^2(.)$ is the process variance, ρ_ϕ is a valid correlation function, and the correlation between W_i and W_j, for every $s_i,\ s_j \epsilon\ G$, is defined as

$$\rho_\phi(s_j,\ s_k) = \sqrt{v_j v_k}\rho_\phi(|d(\ s_j) - d(\ s_k)|),$$

where $v_j = v(s_j)$ is the variance of W_j and d is a function that maps the original coordinates of the G space to a new D space in which the isotropy assumption is satisfied [83].

2.3.3. Parameter Interpretation

Goel processes have been used in the modeling of counting data for various environmental applications [64,81], mostly due to their versatility in the modeling of various behaviors of the intensity function of nonhomogeneous Poisson processes. For example, for $\alpha \leq 1$, the function λ decreases; for some combinations of $\alpha = 1$ and near-zero β values, the function λ is approximately constant (homogeneous Poisson process); for $\alpha > 1$, the function λ can only increase in the $(0, T]$ interval; or in other configurations, the function λ can only increase until a certain threshold value t^* and then it shifts its trend. The calculation of the change point t^* is performed using the following Expression (2).

$$t^* = \left((\alpha - 1)/\alpha\beta)^{1/\alpha}\right). \tag{2}$$

Another advantage of this model is the interpretation of parameters. For example, the vector of regression coefficients Ψ measures the linear association of covariables X in explaining the spatial variability of the mean process. On the other hand, ϕ, v and d model the covariance structure of the spatial process.

2.3.4. Spatial Interpolation of the R10 mm, R20 mm and R* Indices

Let $A_l = [\tau_{l-1}, \tau_l), \tau_0 = 1,\ l = 1, \ldots, L$, be the time intervals in the year l, L the number of years, and , N_l the number of days in the interval l. The R10 mm index for any $s \in G$ in year l is given by

$$R10mm_l(\theta \mid s, A_l) = \frac{m(s, \tau_l \mid \theta) - m(s, \tau_{l-1} \mid \theta)}{N_l}$$

where θ is the set of parameters of the model proposed by Morales and Vicini (2020) [81] and $m(s,\ t)$ defined in (1) is the number of days with daily precipitation higher than 10 mm. Thus, the expected value of R10 mm is

$$E(R10mm_l(\theta \mid s, A_l) \mid D) = \int_\theta R10mm_l(\theta \mid s, A_l)\pi(\theta \mid D)d\theta,$$

$\pi(\theta \mid D)$ is the posterior distribution of θ.

The estimation of the R20 mm index is analogous to that of the R10 mm index.

The R* index for $s \in G$ in year l is given by

$$R_l^*(\theta \mid s, A_l) = \frac{m(s, \tau_l \mid \theta) - m(s, \tau_{l-1} \mid \theta)}{N_l}$$

where $m(s,\ t)$ is the number of days in which daily precipitation exceeded P_{95}. Thus, the expected value of R* in year l is given by

$$E(R_l^*(\theta \mid s, A_l) \mid D) = \int_\theta R_l^*(\theta \mid s, A_l)\pi(\theta \mid D)d\theta,$$

The details of the spatial interpolation of $m(s,\ t)$ are fully described in Morales et al. [64] and Morales and Vicini [81].

3. Results and Discussion

3.1. NC Subregion

3.1.1. Results Obtained for the R10 mm Index

Among the results of the model adjusted to estimate the R10 mm index, we highlight that α is significantly larger than 1, which indicates statistical evidence that the occurrence of rainfall above 100 mm appears not to be constant (see Table 1). In other words, the incidence rate of this type of event increases until 26 March 1992 and then starts decreasing. The 95% confidence interval for this change point is found between 23 February 1989 and 29 September 1994. Another important result is that latitude seems to be an important aspect explaining the R10 mm index. By moving north from NEB toward the equator, the R10 mm index seems to decrease (see Figure 2). In Figure 2, one can notice that in the year 1991, the proportion of R10 mm is higher for locations near the coastline, with values ranging from 0.13 to 0.18. Locations farther from the coastline present R10 mm proportions varying from 0.10 to 0.13. This spatial variability regarding the proportion of the R10 mm index did not significantly change in the other years (see the space–time behavior of the R10 mm index in the Supplementary Material). Rainfall over this region is caused mainly by easterly wave disturbances (EWD) [84].

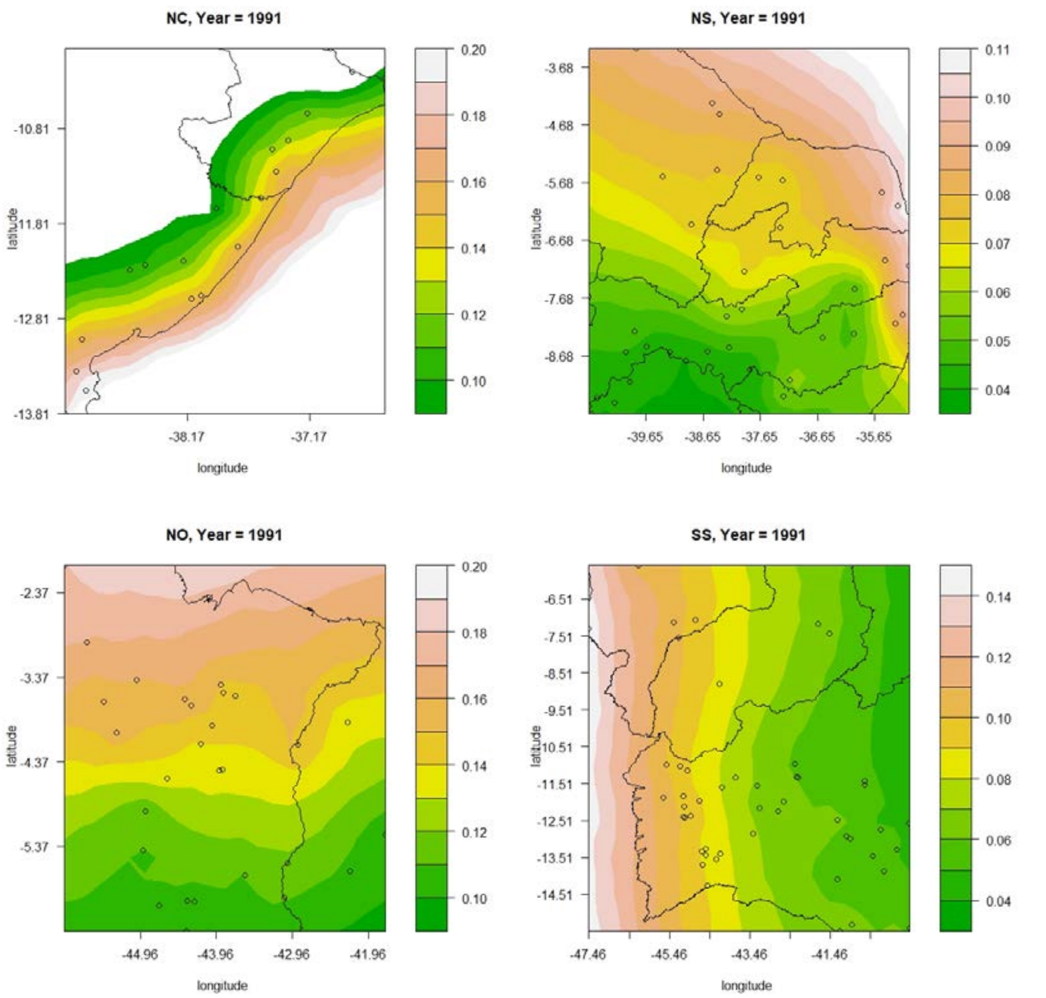

Figure 2. *Cont.*

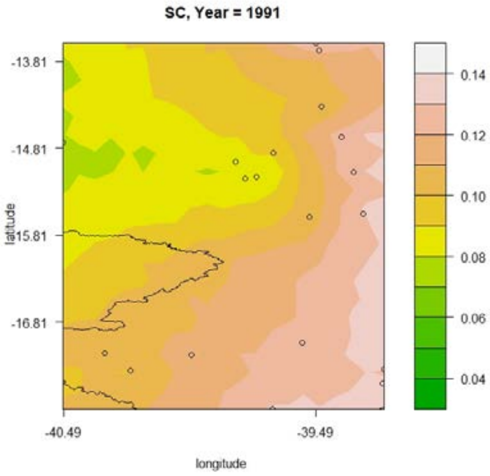

Figure 2. Predictions of rainfall relative frequency that exceeded the 10 mm threshold in the NC, NS, NO, SS and SC regions in 1991.

Table 1. Posterior mean, median and 95% credibility interval for the parameters β, α, ϕ, $\sigma 2$ and $\Psi' = (\Psi_0, \Psi_1, \Psi_2)$ (Ψ_0 is the intercept, Ψ_1 is the coefficient associated with longitude and Ψ_2 is the coefficient associated with latitude) of the model adjusted for an estimate of the R10 mm index in the NC, NS, NO, SS and SC regions.

Subregion	Parameter	Mean	50%	2.5%	97.5%
NC	β	6.42×10^{-6}	6.38×10^{-6}	5.86×10^{-6}	7.11×10^{-6}
	α	1.04	1.04	1.03	1.05
	ϕ	0.33	0.13	0.01	1.18
	Ψ_0	14.93	14.81	4.63	26.44
	Ψ_1	0.30	0.30	−0.04	0.66
	Ψ_2	−0.49	0.50	−0.78	−0.19
NS	β	1.42×10^{-5}	1.41×10^{-5}	1.24×10^{-5}	1.61×10^{-5}
	α	1.01	1.01	1.00	1.03
	ϕ	0.26	0.12	0.01	0.96
	Ψ_0	10.39	10.38	6.77	14.20
	Ψ_1	0.04	0.04	$^{-}$.05	0.13
	Ψ_2	0.10	0.10	0.02	0.19
NO	β	8.08×10^{-6}	8.09×10^{-6}	7.23×10^{-6}	8.77×10^{-6}
	α	1.02	1.02	1.01	1.03
	ϕ	0.29	0.16	0.01	0.96
	Ψ_0	8.74	8.78	5.62	11.55
	Ψ_1	−0.03	−0.03	−0.09	0.03
	Ψ_2	0.13	0.13	0.60	0.20
SS	β	9.22×10^{-6}	9.18×10^{-6}	8.38×10^{-6}	1.03×10^{-5}
	α	1.00	1.00	0.99	1.01
	ϕ	0.07	0.04	0.01	0.33
	Ψ_0	1.75	1.67	0.00	3.74
	Ψ_1	−0.17	−0.17	−0.20	−0.13
	Ψ_2	0.00	0.00	−0.03	0.04
SC	β	1.28×10^{-5}	1.27×10^{-5}	1.15×10^{-5}	1.41×10^{-5}
	α	1.00	1.00	0.98	1.01
	ϕ	0.19	0.07	0.01	0.75
	Ψ_0	16.74	17.00	6.15	26.84
	Ψ_1	0.20	0.20	−0.06	0.44
	Ψ_2	−0.03	−0.02	−0.20	0.11

3.1.2. Results Obtained for the R20 mm Index

Table 2 shows that the α parameter is significantly larger than 1 in the NC and NO regions, and thus, in the NC region, the rate of occurrence of rainfall surpassing 20 mm increases until 3 October 1989 and then decreases, with the 95% confidence interval located between 22 September 1983 and 16 February 1994 for this change point. Conversely, in region NO, the rate of occurrence of rainfall surpassing 20 mm increases until 6 June 1985 and then decreases, with the 95% confidence interval located between 29 August 1982 and 2 April 1988 for this change point. The estimated change point and its respective credibility interval are calculated by substituting the α and β values obtained in the estimation process into Equation (2).

Table 2. Posterior mean, median and 95% credibility interval for the parameters β, α, ϕ, $\sigma 2$ and $\Psi' = (\Psi_0, \Psi_1, \Psi_2)$ (Ψ_0 is the intercept, Ψ_1 is the coefficient associated with longitude and Ψ_2 is the coefficient associated with latitude) of the model adjusted for an estimate of the R20 mm index in the NC, NS, NO, SS and SC regions.

Subregion	Parameter	Mean	50%	2.5%	97.5%
NC	β	7.25×10^{-6}	7.23×10^{-6}	5.93×10^{-6}	8.73×10^{-6}
	α	1.03	1.03	1.01	1.05
	ϕ	0.6	0.19	0.01	2.12
	Ψ_0	16.84	17.04	4.20	28.80
	Ψ_1	0.40	0.41	0.00	0.81
	Ψ_2	−0.59	−0.60	−0.92	−0.22
NS	β	8.27×10^{-6}	8.17×10^{-6}	6.99×10^{-6}	1.02×10^{-5}
	α	1.01	1.01	0.99	1.03
	ϕ	0.25	0.13	0.01	0.84
	Ψ_0	9.43	9.55	3.36	14.54
	Ψ_1	0.02	0.02	−0.12	0.15
	Ψ_2	0.08	0.08	−0.02	0.19
NO	β	9.82×10^{-6}	9.72×10^{-6}	8.61×10^{-6}	1.15×10^{-5}
	α	1.02	1.02	1.01	1.04
	ϕ	0.40	0.17	0.01	1.29
	Ψ_0	8.04	7.98	4.58	11.66
	Ψ_1	−0.03	−0.03	−0.10	0.06
	Ψ_2	0.11	0.11	0.02	0.20
SS	β	1.65×10^{-5}	1.65×10^{-5}	1.42×10^{-5}	1.87×10^{-5}
	α	0.98	0.98	0.97	0.99
	ϕ	0.06	0.03	0.01	0.22
	Ψ_0	0.27	0.27	−1.86	2.37
	Ψ_1	−0.18	−0.18	−0.22	−0.13
	Ψ_2	0.01	0.01	−0.04	0.05
SC	β	1.20×10^{-5}	1.19×10^{-5}	9.57×10^{-6}	1.46×10^{-5}
	α	0.97	097	0.95	0.99
	ϕ	1.13	0.25	0.01	4.92
	Ψ_0	15.25	15.45	5.72	25.48
	Ψ_1	0.22	0.23	−0.02	0.47
	Ψ_2	−0.13	−0.13	−0.27	0.01

Latitude also significantly explains the mean R20 mm values, which also decrease the more we displace north from NEB toward the Equator (see Figure 3). Figure 3 shows the estimated surface for the proportion of days in which rainfall exceeded 20 mm for the year 1991, and one can notice that the proportion of the R20 mm index is higher in locations near the coast, with values ranging from 0.03 to 0.05. Maximum rainfall in this region occurs between April and July, while in locations farther from the coast, the R20 mm proportions vary from 0.02 to 0.03.

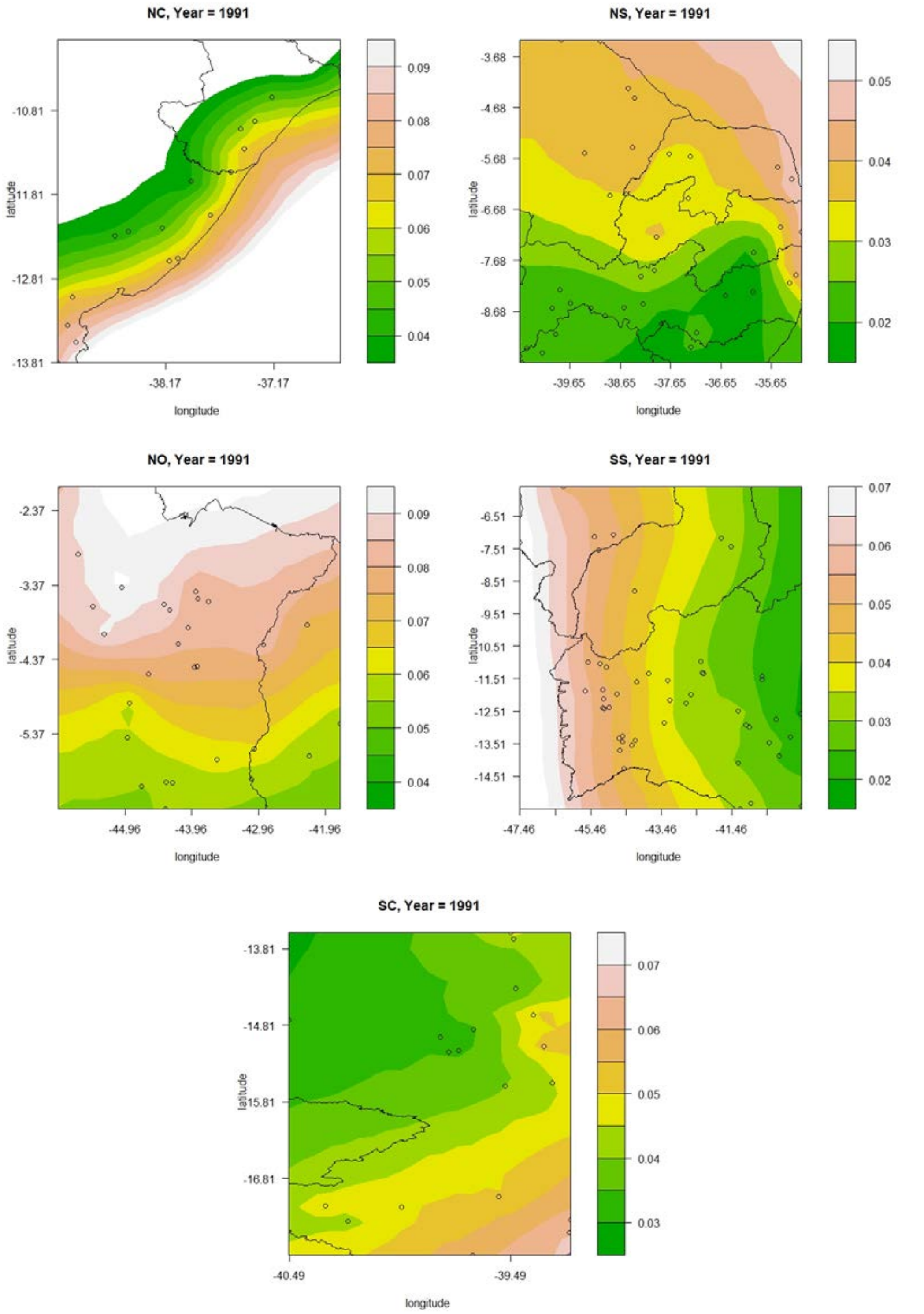

Figure 3. Predictions of rainfall relative frequency that exceeded the 20 mm threshold in the NC, NS, NO, SS and SC regions in 1991.

The surfaces estimated for the R20 mm index in other years presented a similar trend and behavior compared to 1991 (see the space–time behavior of the R20 mm index in the Supplementary Material). The spatial correlation of R20 mm indices between locations separated by at least 9.7 km is 0.95; the spatial correlation of R20 mm indices between locations separated by 190 km is 0.36; and the spatial correlation of R20 mm indices between locations separated by 498 km is 0.07 (see Figure 4). Overall, the spatial correlation for this index was anisotropic.

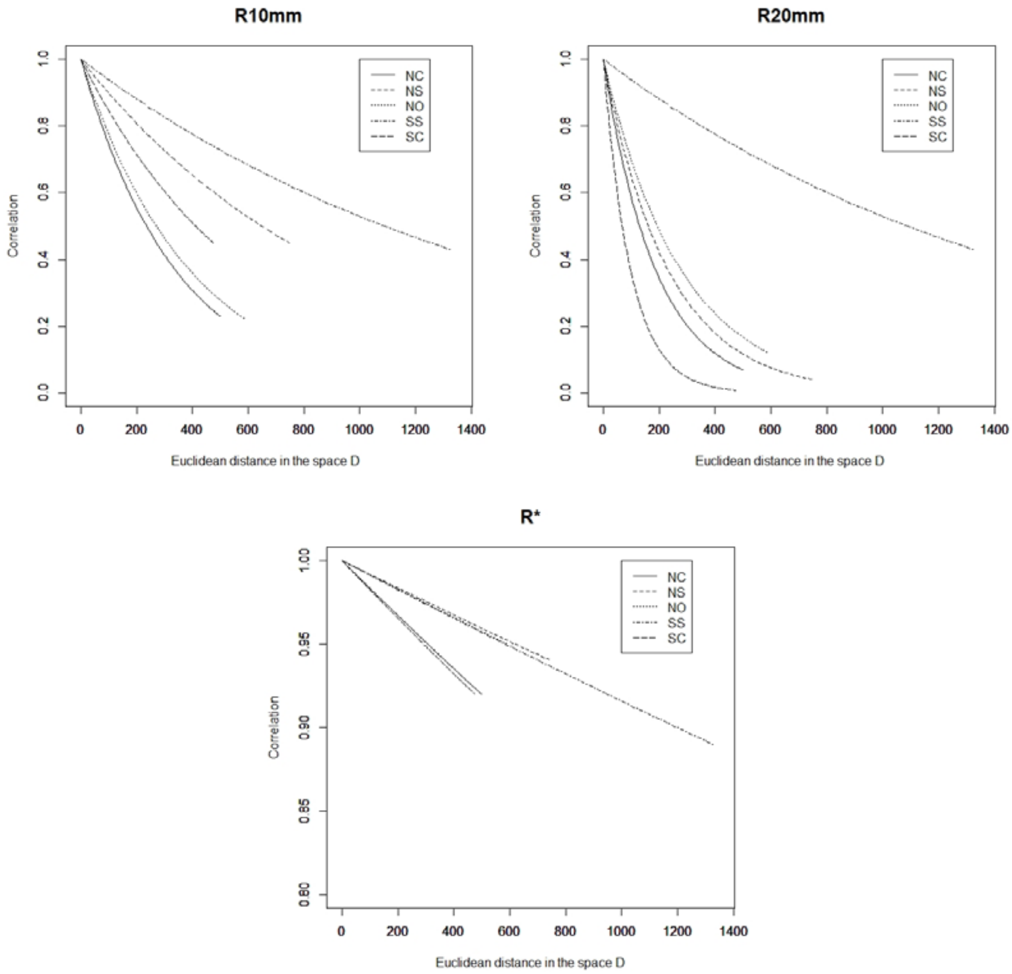

Figure 4. Correlation function estimated for each index and region. Scale of Euclidean distances measured in kilometers.

3.1.3. Results Obtained for the R* mm Index

Table 3 shows that the α parameter is significantly larger than 1, and thus, the occurrence of rainfall exceeding the 95th percentile increases until 23 January 1990 and then decreases, with the 95% confidence interval located between 4 October 1987 and 29 October 1992 for this change point. Longitude and latitude are not significant in explaining the mean R* value, and the estimated surface for this index is homogeneous, with a proportion of rainfall exceeding the 95th percentile ranging from 0.051 to 0.052 in 1991. The estimated surface for the R* index changed each year and was significantly higher than 0.05 in 1989, 1990 and 1991 (see the space–time behavior of the R* index in the Supplementary Material). The spatial correlation for the R* index is anisotropic (see Figure 5). In the NC region, daily rainfall exceeding the 95th percentile is higher than 100 mm/day on average during the period from March to May [7]. The National Center for Natural Disaster Monitoring and Alerts (CEMADEN—Centro Nacional de Monitoramento e Alertas de Desastres Naturais) registered more than 10 natural disasters associated with heavy rainfall in the city of Maceió, located at the coast of the state of Alagoas, from January 2016 until February 2019 [7]. This is quite concerning since the R* index varies from 0.04 to 0.06 over the NC region during the studied period. The spatial correlation of the R* indices between locations is generally strong; for example, the spatial correlation between locations separated by at least 9.7 km is 0.99; the spatial correlation of R* indices between locations separated by 190 km is 0.96; and the spatial correlation of R* indices between locations separated by 498 km is 0.92 (see Figure 4).

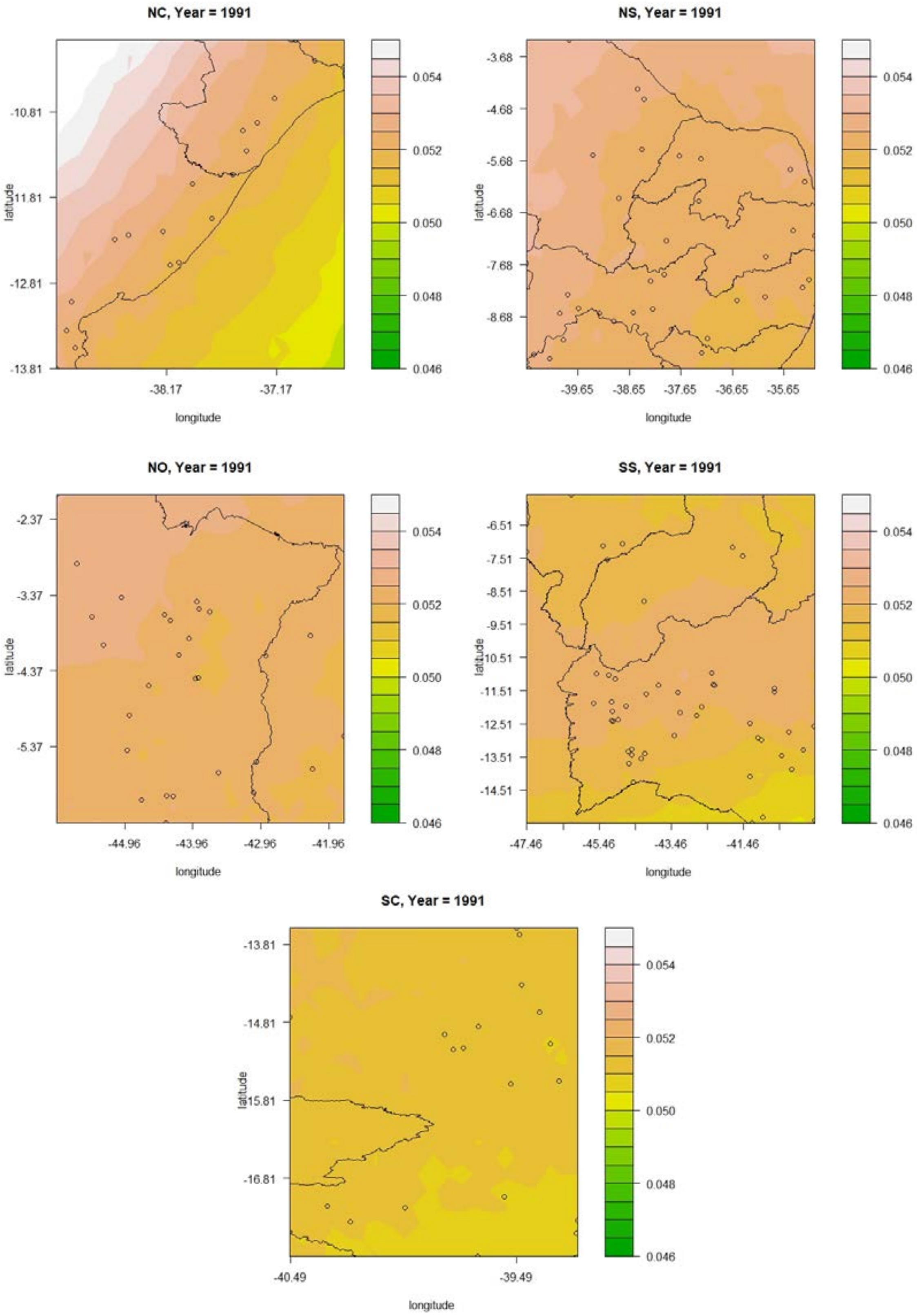

Figure 5. Predictions of rainfall relative frequency that exceeded 95th threshold in the NC, NS, NO, SS and SC regions in 1991.

Table 3. Posterior mean, median and 95% credibility interval for the parameters β, α, ϕ, $\sigma 2$ and $\Psi' = (\Psi_0, \Psi_1, \Psi_2)$ (Ψ_0 is the intercept, Ψ_1 is the coefficient associated with longitude and Ψ_2 is the coefficient associated with latitude) of the model adjusted for an estimate of the R* mm index in the NC, NS, NO, SS and SC regions.

Subregion	Parameter	Mean	50%	2.5%	97.5%
NC	β	1.03×10^{-5}	1.03×10^{-5}	8.31×10^{-6}	0.21×10^{-5}
	α	1.07	1.07	1.06	1.10
	ϕ	0.02	0.01	0.01	0.05
	Ψ_0	7.16	6.94	4.19	11.33
	Ψ_1	−0.02	−0.03	−0.12	0.12
	Ψ_2	0.01	0.02	−0.08	0.08
NS	β	1.44×10^{-5}	1.42×10^{-5}	1.28×10^{-5}	1.62×10^{-5}
	α	1.05	1.05	1.04	1.07
	ϕ	0.01	0.01	0.01	0.03
	Ψ_0	7.78	7.76	7.11	8.59
	Ψ_1	0.00	0.00	−0.02	0.02
	Ψ_2	0.01	0.01	0.00	0.02
NO	β	1.36×10^{-5}	1.37×10^{-5}	1.15×10^{-5}	1.54×10^{-5}
	α	1.06	1.06	1.05	1.08
	ϕ	0.01	0.01	0.01	0.04
	Ψ_0	7.66	7.66	6.67	8.55
	Ψ_1	0.00	0.00	−0.02	0.02
	Ψ_2	0.00	0.00	−0.02	0.02
SS	β	2.08×10^{-5}	2.06×10^{-5}	1.82×10^{-5}	2.39×10^{-5}
	α	1.02	1.02	1.01	1.04
	ϕ	0.01	0.01	0.01	0.02
	Ψ_0	7.68	7.71	7.05	8.14
	Ψ_1	0.00	0.00	−0.01	0.01
	Ψ_2	0.00	0.00	−0.01	0.01
SC	β	1.60×10^{-5}	1.61×10^{-5}	1.35×10^{-5}	1.80×10^{-5}
	α	0.98	0.98	0.97	1.00
	ϕ	0.02	0.01	0.01	0.05
	Ψ_0	8.08	8.01	5.88	10.76
	Ψ_1	−0.01	−0.01	−0.06	0.05
	Ψ_2	0.00	0.00	−0.02	0.03

3.2. NS Subregion

3.2.1. Results Obtained for the R10 mm Index

Table 1 shows the summary of posterior distributions for the β, α, φ and Ψ parameters. The results showed that α is significantly equal to 1, indicating that the occurrence of rainfall exceeding 10 mm decreases with time. Additionally, latitude seems to be an important variable explaining the variability of the R10 mm index, which increases further north toward the Equator. This trend can be observed in the estimated surface for the R10 mm index in the year 1991, as shown in Figure 2. One can observe that the highest relative frequencies occur at the coast of the Pernambuco, Paraíba, Rio Grande do Norte and Ceará states, with values ranging from 0.09 to 0.10. On the other hand, the variability of the relative frequency in the inlands of this subregion varies from 0.04 to 0.08. The behavior of the relative frequency surface of rainfall exceeding 10 mm varies with time and decreases in the inlands of the region (see the space–time behavior of the R10 mm index in the Supplementary Material). Rainfall in this region is mainly driven by the displacement of the Intertropical Convergence Zone (ITCZ) toward the Southern Hemisphere during autumn, which characterizes the wet season in the region [21]. Figure 6 shows a spatial deformation in the inlands of the Paraíba and Pernambuco states, indicating an anisotropic spatial correlation function. A possible explanation for this deformation may be associated with the fact that his region is surrounded by the Borborema Plateau in the Paraíba and

Pernambuco states, with altitudes reaching more than 1000 m. The spatial correlation of R10 mm indices between locations separated by at least 14 km (minimum distance between gauges) is 0.97; the spatial correlation of R10 mm indices between locations separated by 343 km (mean distance between gauges) is 0.70; and the spatial correlation of R10 mm indices between locations separated by 747 km (maximum distance between gauges) is 0.45 (see Figure 4).

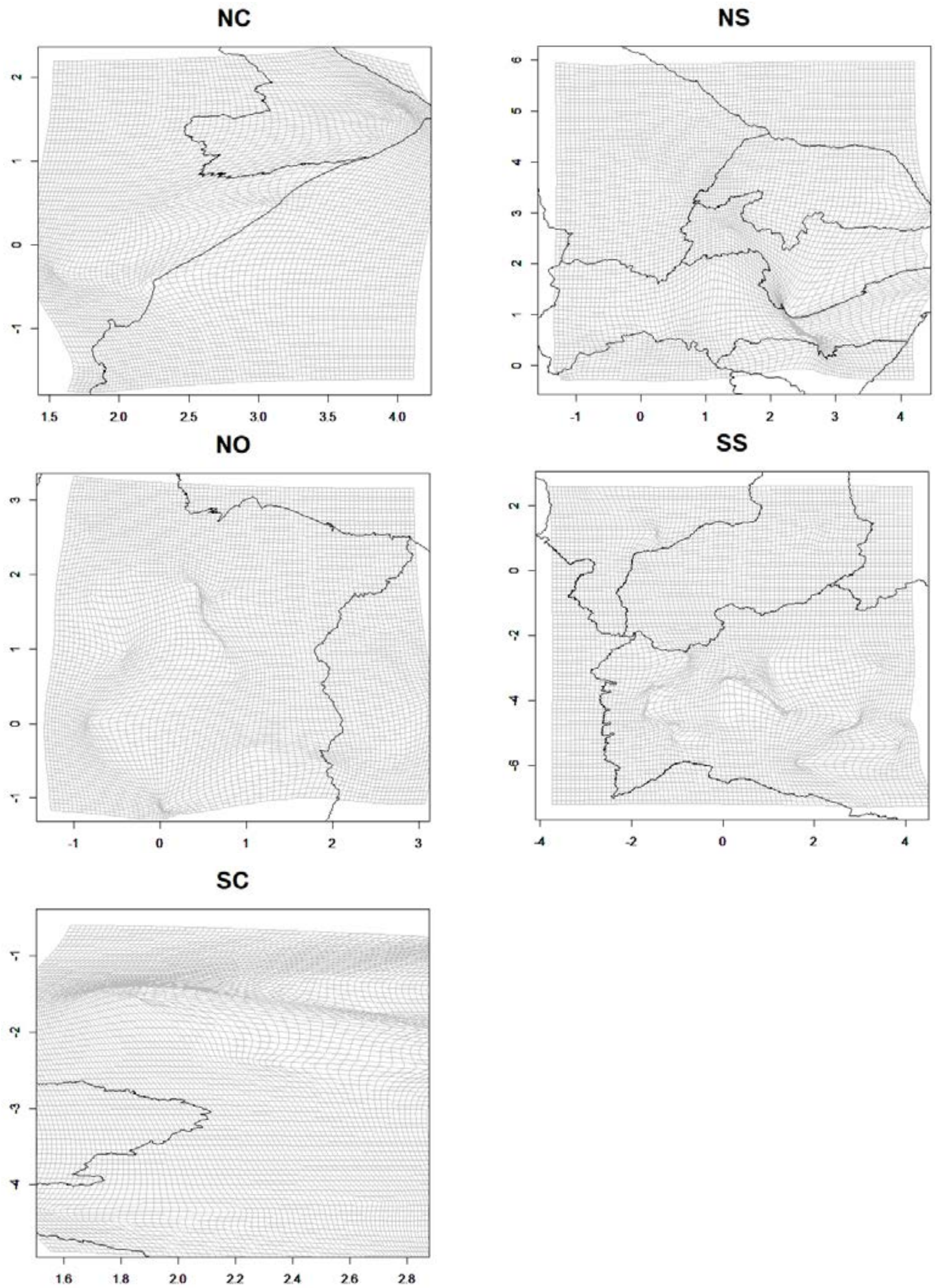

Figure 6. Spatial estimation of D in the NC, NS, NO, SS and SC regions. The horizontal and vertical lines represent a fine grid representing the area of interest. The angle of intersection between the horizontal and vertical lines should be 90 degrees when the spatial process is isotropic. Otherwise, the spatial process will be anisotropic.

3.2.2. Results Obtained for the R20 mm Index

The results for the R20 mm index are similar to those of the R10 mm index. For example, the estimated model also retrieved an α parameter significantly equal to 1, which indicates a negative trend for the occurrence of rainfall exceeding 20 mm. Additionally, latitude and longitude did not significantly explain the variability in the R20 mm index, and thus, the spatial dependence for this index is explained solely by the spatial correlation function (see Table 2). Although latitude is not significant, the estimated surface shows that the relative frequency of rainfall exceeding 20 mm in the year 1991 is higher at the coast of the region, with values ranging from 0.035 to 0.045, where the occurrence of more intense precipitation events is expected [7]. Maximum rainfall values in this region occur between April and July [85]. In the semiarid inlands of this subregion, however, the relative frequency of rainfall exceeding 20 mm varies from 0.010 to 0.035. A decrease with time in the R20 mm index is observed in the inlands of the subregion (see the space–time behavior of the R20 mm index in the Supplementary Material). The estimates for the spatial deformation and the ϕ parameter are similar to those obtained for the R10 mm model. Thus, the spatial correlation function has the same behavior as the function for the R10 mm index, as previously described.

3.2.3. Results Obtained for the R* mm Index

The α parameter is significantly larger than 1, which indicates that the occurrence of rainfall events exceeding the 95th percentile increases until 19 June 1986 and then decreases (change point). The 95% confidence interval for precipitation is located between 4 December 1984 and 11 December 1987. Figure 5 shows the R* estimates for 1991, and the space–time behavior of this index is presented in detail in the Supplementary Materials section. Neither latitude nor longitude significantly explained the variability in the R* index, which indicates that the spatial dependence is explained solely by the spatial correlation function (see Table 3). The results show that the relative frequency of rainfall events exceeding the 95th percentile in the years from 1984 to 1988 is significantly larger than 0.05, and in the years from 2008 to 2010, it is significantly lower than 0.05 (see Supplementary Materials). The highest values for the index can be found in the coastal region. Daily accumulated rainfall can exceed 120 mm/day [86]. In Natal, a city located over the eastern coast of the NS region, the probability of occurrence of precipitation higher than 40 mm/day in June is 90.8% [7].

According to Kousky [87], Zhou and Lau [88] and Rodrigues et al. [19], the coastal region of NEB is where the highest annual accumulated precipitation is registered. One can also observe an anisotropic spatial correlation between the R10 mm index values over this region. Figure 6 shows this deformation of the original spatial characteristics at points near the coast. A possible explanation might be related to the presence of several topographic features near this deformation, such as the Diamantina Plateau reaching up to 2033 m in altitude. The spatial correlation of R10 mm indices between locations separated by at least 9.7 km (minimum distance between gauges) is 0.97; the spatial correlation of R10 mm indices between locations separated by 190 km (mean distance between gauges) is 0.57; and the spatial correlation of R10 mm indices between locations separated by 498 km (maximum distance between gauges) is 0.23 (see Figure 4). Figure 4 shows a strong spatial correlation for the R* index, with values of approximately 0.99 between locations separated by 14 km; the spatial correlation of R* indices between locations separated by 343 km is 0.97; and the spatial correlation of R* indices between locations separated by 747 km is 0.94 (see Figure 4).

3.3. NO Subregion

3.3.1. Results Obtained for the R10 mm Index

Table 1 shows that the value of α is significantly larger than 1, which indicates that the occurrence of rainfall exceeding 10 mm increases until 24 April 1986 and then decreases, with the 95% confidence interval for the change point located between 24 August 1983 and

17 September 1989. Latitude significantly explains the variability of the R10 mm index, which increases in locations further north of NEB. For example, Figure 2 shows that for the year 1991, the relative frequency values in the northern portion of the subregion varied from 0.14 to 0.19, while in the southern portion, they varied from 0.10 to 0.14. The NO region presents the highest accumulated rainfall values in NEB, which may be associated with its proximity to the Amazon region [21]. In the Supplementary Materials, one can observe the small variability in the space–time trends of the R10 mm index. On the other hand, Figure 6 shows a deformation in the original space, suggesting that the spatial correlation is anisotropic. It is worth highlighting that this deformation comprises an area with three biomes with contrasting characteristics: the Amazon rainforest, the Cerrado (Brazilian savanna) and the Caatinga (dry forest), with accumulated rainfall ranging from 700 mm (Caatinga and Cerrado) to 5000 mm (Amazon). This factor associated with the main meteorological systems acting over this region may explain the deformations found [81]. The spatial correlation of R10 mm indices between locations separated by at least 5.6 km (minimum distance between gauges) is 0.99; the spatial correlation of R10 mm indices between locations separated by 214 km (mean distance between gauges) is 0.57; and the spatial correlation of R10 mm indices between locations separated by 590 km (maximum distance between gauges) is 0.22 (see Figure 4).

3.3.2. Results Obtained for the R20 mm Index

Table 2 shows that the α parameter is significantly larger than 1, and thus, the occurrence of rainfall exceeding 20 mm increases until 6 June 1985 and then decreases, with the 95% confidence interval for this change point located between 28 August 1982 and 2 April 1988. The coefficient associated with latitude is significant in explaining the mean R20 mm index value, which is positive and increases when latitude decreases (see Figure 3). The northern coast presents the highest annual accumulated rainfall [19,30], when compared to other NEB regions. The wet season occurs between February and May [19]. Figure 3 shows the estimated surface for the proportion of days that exceed the 20 mm rainfall threshold in the year 1991. One can observe that the R20 mm proportion is higher in the northern portion of the subregion and near the coast, with values ranging from 0.065 to 0.090. Locations farther from the coast present proportions that vary from 0.040 to 0.065. The surfaces estimated for the R20 mm index in other years present a similar behavior (see the space–time behavior of the R20 mm index in the Supplementary Material). The spatial correlation for the R20 mm index was anisotropic (see Figure 6). The spatial correlation of R20 mm indices between locations separated by at least 5.6 km is 0.98; the spatial correlation of R20 mm indices between locations separated by 214 km is 0.46; and the spatial correlation of R20 mm indices between locations separated by 590 km is 0.12 (see Figure 4).

3.3.3. Results Obtained for the R* Index

The α parameter is significantly larger than 1, which indicates that the occurrence of rainfall events exceeding the 95th percentile increases until 5 March 1987 and then decreases (change point). The 95% confidence interval for precipitation is located between 17 August 1985 and 18 April 1989. Figure 5 shows R* estimates for the year 1991, which varies smoothly at approximately 0.052. The results for the northern NEB coast were similar to the results for the eastern coast, with high rainfall rates. Values higher than 100 mm/day are expected every two years [7]. Approximately 14 cities in this region suffered from hydrological natural disasters classified as floods, landslides or flash floods [7]. In the Supplementary Materials section, one can observe the spatial and temporal behavior of the R* index. Neither latitude nor longitude are significant in explaining the variability of the index, which indicates that the spatial dependence is explained solely by the spatial correlation function (see Table 3). The relative frequency of rainfall exceeding the 95th percentile in the years 1984 to 1987 is significantly larger than 0.05. For the years from 2008 to 2010, however, R* is significantly lower than 0.05 in this region (see Supplementary Materials). Figure 4 shows a strong spatial correlation for the R* index, with values of approximately

0.99 between locations separated by 5.6 km; the spatial correlation of R* indices between locations separated by 214 km is 0.98; and the spatial correlation of R* indices between locations separated by 590 km is 0.95 (see Figure 4).

3.4. SS Subregion

3.4.1. Results Obtained for the R10 mm Index

Among the results shown in Table 1, it is worth highlighting that the α parameter is significantly equal to 1, which indicates that the occurrence of rainfall exceeding 10 mm decreases with time. Another observed result is that the longitude coefficient significantly explains the variability of the R10 mm index, which is negative and therefore increases in value when moving westward in the subregion. This behavior can be observed by analyzing the estimated surface for the R10 mm index in the year 1991, as presented in Figure 2, which shows higher relative frequencies ranging from 0.08 to 0.14 in the western SS subregion. At the eastern portion of the subregion, the relative frequency is lower, varying from 0.04 to 0.08. Additionally, this behavior presents little temporal variability (see the space–time behavior of the R10 mm index in the Supplementary Material). This region is under the influence of a semiarid climate, with generally low rainfall values [19,86,89]. The wet season occurs between December and February. The main atmospheric systems causing maximum seasonal rainfall over the region are the SACZ [71,72] and UTCV. Figure 6 shows a spatial deformation in the inlands of Bahia state, indicating that the spatial correlation function is anisotropic. From a topographic perspective, a potential explanation for this deformation over this particular region is the fact that it is located in the Mangabeiras Plateau and the Goiás Serra Geral mountain range, which encompass a wide area west of Bahia state with altitudes reaching up to 800 m. A positive trend in R10 mm values can be observed for 1991, as shown in Figure 2. The spatial correlation of R10 mm indices between locations separated by at least 4 km (minimum distance between gauges) is 0.99; the spatial correlation of R10 mm indices between locations separated by 420 km (mean distance between gauges) is 0.77; and the spatial correlation of R10 mm indices between locations separated by 1326 km (maximum distance between gauges) is 0.43 (see Figure 4).

3.4.2. Results Obtained for the R20 mm Index

The results shown in Table 2 indicate that the α parameter is significantly smaller than 1, which in turn suggests that the occurrence of rainfall exceeding 20 mm is decreasing over time. This result raises concerns since this region already presents low precipitation rates [19,21]. The results were similar to those found for the R10 mm index, with the longitude coefficient significantly explaining the variability of the R20 mm index, which is also negative and therefore indicates increasing values in the western portion of the subregion. This portion comprises part of the MATOPIBA (Maranhão, Tocantins, Piauí and Bahia states) region, which is widely covered by soybean croplands [90]. The positive trend in R20 mm index values can be observed for the year 1991 in Figure 2, which shows that the higher relative frequencies range from 0.04 to 0.06, while in the eastern portion of the subregion, they vary from 0.02 to 0.04. The behavior of the spatial correlation function is similar to that found for the R10 mm index, which was described in the previous paragraph.

3.4.3. Results Obtained for the R* Index

The α parameter is significantly smaller than 1, which indicates that the occurrence of rainfall events exceeding the 95th percentile decreases with time. Figure 5 shows the estimates for the R* index in the year 1991, when its values varied smoothly at approximately 0.052. The spatial and temporal behavior of this index can be observed in the Supplementary Materials section. Neither latitude nor longitude were significant in explaining the variability of the R* index, which indicates that its spatial dependence is dictated by the spatial correlation function (see Table 3). It is also noteworthy that the relative frequency of rainfall exceeding the 95th percentile from 1980 to 1987 is significantly larger than 0.05. For the years from 2000 to 2010, however, R* is significantly lower than 0.05 in this region (see Supplementary Materials).

Figure 4 shows a strong spatial correlation for the R* index, with values of approximately 0.99 between locations separated by 4 km; the spatial correlation of R* indices between locations separated by 420 km is 0.96; and the spatial correlation of R* indices between locations separated by 1326 km is 0.89 (see Figure 4).

3.5. SC Subregion

3.5.1. Results Obtained for the R10 mm Index

Among the results obtained for the SC subregion, it is worth highlighting that the α parameter is significantly lower than 1, indicating that the occurrence of rainfall exceeding 10 mm decreases with time. Another important result refers to the coefficients associated with latitude and longitude, which were not significant in explaining the variability of the R10 mm index. Thus, spatial variability is explained solely by the spatial correlation function (see Table 1). Figure 2 shows the estimated surface for R10 mm values in the year 1991. The highest relative frequencies occur in the eastern portion of the subregion, with values ranging from 0.10 to 0.14. On the other hand, the variability in the relative frequency in the western portion varies from 0.04 to 0.10. The SC subregion comprises the southern coast of Bahia state, where rainfall does not vary much throughout the year but higher volumes are registered in November. The wet season in this region occurs during summer [21]. Rainfall is mainly modulated by the SACZ [71,72]. The behavior of the relative frequency surface of rainfall exceeding 10 mm presents some temporal variability (see the space–time behavior of the R10 mm index in the Supplementary Material). In Figure 6, one can notice a spatial deformation at the southern portion of the region, indicating that the spatial correlation is anisotropic. The topographical explanation is analogous to that of the NC region, since both subregions are relatively close to the previously described plateaus and topographic features. The spatial correlation of R10 mm indices between locations separated by at least 5 km (minimum distance between gauges) is 0.99; the spatial correlation of R10 mm indices between locations separated by 192 km (mean distance between gauges) is 0.72; and the spatial correlation of R10 mm indices between locations separated by 474 km (maximum distance between gauges) is 0.45 (see Figure 4).

3.5.2. Results Obtained for the R20 mm Index

The results obtained for the R20 mm index are similar to those referring to the R10 mm index. For example, the α parameter is significantly lower than 1, indicating that the occurrence of rainfall exceeding 20 mm decreases with time. Similarly, the coefficients related to longitude and latitude were not significant, and thus spatial variability is explained solely by the spatial correlation function (see Table 2). However, the behavior of the spatial correlation function is different for the R20 mm index. The spatial correlation of R20 mm indices between locations separated by at least 5 km is 0.95; the spatial correlation of R20 mm indices between locations separated by 192 km is 0.14; and the spatial correlation of R20 mm indices between locations separated by 474 km is 0.01 (see Figure 4).

3.5.3. Results Obtained for the R* Index

The α parameter is significantly lower than 1, which indicates that the occurrence of rainfall events exceeding the 95th percentile decreases with time. Figure 5 shows that the estimates for the R* index in 1991 vary smoothly at approximately 0.052. In the Supplementary Materials section, one can observe the spatial and temporal behavior of this index. Neither latitude nor longitude was significant in explaining the variability of the R* index, and therefore, it is explained solely by the spatial correlation function (see Table 3). Figure 4 shows a strong spatial correlation for the R* index, with values of approximately 0.99 between locations separated by 5 km; the spatial correlation of R* indices between locations separated by 192 km is 0.96; and the spatial correlation of R* indices between locations separated by 474 km is 0.92 (see Figure 4).

4. Conclusions

Studies analyzing extreme precipitation events are of uttermost importance, especially because of the potential impacts caused by such events. The objective of this study was to model the number of days with precipitation exceeding 10 mm, 20 mm and the 95th percentile in various regions of Northeast Brazil by using a statistical model for space–time counting. Through this approach, it was possible to analyze the frequency of extreme rainfall events while also considering temporal and spatial variability in NEB. Overall, the results indicate that the estimates for the occurrence of extreme events depend on the studied period and location. The eastern coast was the NEB region with the highest count of events. The semiarid region, on the other hand, presented the lowest count. In 1991, the occurrence of rainfall exceeding 10 mm/day varied from 16% to 20% on the eastern coast of the NC subregion. In the semiarid SS subregion, in the same year, the occurrence of rainfall exceeding 10 mm/day was as low as 8%.

By analyzing the results found in this study, we can conclude that the adequate use of the proposed statistical method for space–time counting is promising, with reliable estimations of the frequency of occurrence of extreme precipitation in NEB. The results retrieved by the model were capable of representing the spatial and temporal variability of extreme rainfall in NEB. The results of the space–time analysis of the extreme frequency of rainfall in the Northeast Region of Brazil have several practical applications. They can be used to assist decision makers on a wide range of precipitation-related issues. For example, they can be used to help design stormwater drainage systems that can handle expected precipitation, or to identify areas that are associated with a high risk of natural disasters such as floods and landslides. Furthermore, the results can be used to help water resource managers plan for the effects of extreme rainfall on the region's water supply. It can contribute to identify areas with a high probability of occurrence of water scarcity. The information can also be used to help farmers plan their crop cycles and irrigation practices. Contributing to optimizing crop yields and minimizing losses due to drought or flooding. In general, we strongly believe that the results found in this study can aid in the monitoring and management of water resources by providing crucial information for the formulation of public policies in Northeast Brazil regarding planning, adaptation and mitigation in the face of the risks associated with extreme events, particularly regarding vulnerable populations.

Supplementary Materials: The following supporting information can be downloaded at: https://www.mdpi.com/article/10.3390/atmos14030531/s1, Figures S1–S34.

Author Contributions: Conceptualization, F.E.C.M., D.T.R. and T.V.M.; methodology, F.E.C.M.; software, F.E.C.M. and D.T.R.; validation, A.C.B.A. and C.M.S.e.S.; visualization, F.E.C.M. and T.V.M.; data curation, P.T.d.O., W.A.G. and P.S.L.; writing—original draft preparation, D.T.R.; writing—review and editing, F.E.C.M., D.T.R. and T.V.M.; All authors have read and agreed to the published version of the manuscript.

Funding: This research was funded by National Council for Scientific and Technological Development (CNPq), Process N°405750/2022-6.

Institutional Review Board Statement: Not applicable.

Informed Consent Statement: Not applicable.

Data Availability Statement: The data used in manuscript are available by writing to the corresponding authors.

Acknowledgments: We are thankful to the National Council for Scientific and Technological Development (CNPq) for funding this research.

Conflicts of Interest: The authors declare no conflict of interest.

References

1. Krishnamurti, T.N.; Kishtawal, C.M.; LaRow, T.E.; Bachiochi, D.R.; Zhang, Z.; Williford, C.E.; Gadgil, S.; Surendran, S. Improved Weather and Seasonal Climate Forecasts from multimodel superensemble. *Science* **1999**, *285*, 1548–1550. [CrossRef]
2. Grell, G.A.; Dévényi, D. A Generalized Approach to Parameterizing Convection Combining Ensemble and Data Assimilation Techniques. *Geophys. Res. Lett.* **2002**, *29*, 10–13. [CrossRef]
3. Dantas, V.d.A.; Amorim, A.C.B.; Costa, M.d.S.; Santos e Silva, C.M. Downscaling Dinâmico Sobre o Nordeste Do Brasil Utilizando Um Modelo Climático Regional: Impacto de Diferentes Parametrizações Na Precipitação Simulada. *Rev. Bras. Geogr. Física* **2013**, *6*, 995–1008. [CrossRef]
4. Yang, M.; Tan, Y.; Li, X.; Chen, X.; Zhang, C.; Yu, P. Influence of Cumulus Convection Schemes on Winter North Pacific Storm Tracks in the Regional Climate Model RegCM4.5. *Int. J. Climatol.* **2020**, *40*, 1294–1305. [CrossRef]
5. Wang, Y.; Feng, J.; Luo, M.; Wang, J.; Qiu, Y. Uncertainties in Simulating Central Asia: Sensitivity to Physical Parameterizations Using Weather Research and Forecasting Model. *Int. J. Climatol.* **2020**, *40*, 5813–5828. [CrossRef]
6. Zong, P.; Zhu, Y.; Tang, J. Sensitivity of Summer Precipitation in Regional Spectral Model Simulations over Eastern China to Physical Schemes: Daily, Extreme and Diurnal Cycle. *Int. J. Climatol.* **2019**, *39*, 4340–4357. [CrossRef]
7. Rodrigues, D.T.; Gonçalves, W.A.; Spyrides, M.H.C.; Santos e Silva, C.M.; de Souza, D.O. Spatial Distribution of the Level of Return of Extreme Precipitation Events in Northeast Brazil. *Int. J. Climatol.* **2020**, *40*, 5098–5113. [CrossRef]
8. Caldeira, T.L.; Beskow, S.; Mello, C.R.d.; Faria, L.C.; Souza, M.R.d.; Guedes, H.A.S. Modelagem Probabilística de Eventos de Precipitação Extrema No Estado Do Rio Grande Do Sul. *Rev. Bras. Eng. Agrícola Ambient.* **2015**, *19*, 197–203. [CrossRef]
9. Quadros Gramosa, A.H.; Ferraz do Nascimento, F.; Castro Morales, F.E. A Bayesian Approach to Zero-Inflated Data in Extremes. *Commun. Stat. Theory Methods* **2020**, *49*, 4150–4161. [CrossRef]
10. Gámiz-Fortis, S.R.; Esteban-Parra, M.J.; Trigo, R.M.; Castro-Díez, Y. Potential Predictability of an Iberian River Flow Based on Its Relationship with Previous Winter Global SST. *J. Hydrol.* **2010**, *385*, 143–149. [CrossRef]
11. Paeth, H.; Girmes, R.; Menz, G.; Hense, A. Improving Seasonal Forecasting in the Low Latitudes. *Mon. Weather Rev.* **2006**, *134*, 1859–1879. [CrossRef]
12. Asadieh, B.; Krakauer, N.Y. Global Trends in Extreme Precipitation: Climate Models versus Observations. *Hydrol. Earth Syst. Sci.* **2015**, *19*, 877–891. [CrossRef]
13. Du, H.; Alexander, L.V.; Donat, M.G.; Lippmann, T.; Srivastava, A.; Salinger, J.; Kruger, A.; Choi, G.; He, H.S.; Fujibe, F.; et al. Precipitation from Persistent Extremes Is Increasing in Most Regions and Globally. *Geophys. Res. Lett.* **2019**, *46*, 6041–6049. [CrossRef]
14. Sun, X.; Renard, B.; Thyer, M.; Westra, S.; Lang, M. A Global Analysis of the Asymmetric Effect of ENSO on Extreme Precipitation. *J. Hydrol.* **2015**, *530*, 51–65. [CrossRef]
15. Michaels, P.J.; Knappenberger, P.C.; Frauenfeld, O.W.; Davis, R.E. Trends in Precipitation on the Wettest Days of the Year across the Contiguous USA. *Int. J. Climatol.* **2004**, *24*, 1873–1882. [CrossRef]
16. Bartels, R.J.; Black, A.W.; Keim, B.D. Trends in Precipitation Days in the United States. *Int. J. Climatol.* **2020**, *40*, 1038–1048. [CrossRef]
17. Palharini, R.; Vila, D.; Rodrigues, D.; Palharini, R.; Mattos, E.; Undurraga, E. Analysis of Extreme Rainfall and Natural Disasters Events Using Satellite Precipitation Products in Different Regions of Brazil. *Atmosphere* **2022**, *13*, 1680. [CrossRef]
18. Santos, E.B.; Lucio, P.S.; Santos e Silva, C.M. Seasonal Analysis of Return Periods for Maximum Daily Precipitation in the Brazilian Amazon. *J. Hydrometeorol.* **2015**, *16*, 973–984. [CrossRef]
19. Rodrigues, D.T.; Gonçalves, W.A.; Spyrides, M.H.C.; Santos e Silva, C.M. Spatial and Temporal Assessment of the Extreme and Daily Precipitation of the Tropical Rainfall Measuring Mission Satellite in Northeast Brazil. *Int. J. Remote Sens.* **2019**, *41*, 549–572. [CrossRef]
20. da Cunha Luz Barcellos, P.; Cataldi, M. Flash Flood and Extreme Rainfall Forecast through One-Way Coupling of WRF-SMAP Models: Natural Hazards in Rio de Janeiro State. *Atmosphere* **2020**, *11*, 834. [CrossRef]
21. Oliveira, P.T.; Santos e Silva, C.M.; Lima, K.C. Climatology and Trend Analysis of Extreme Precipitation in Subregions of Northeast Brazil. *Theor. Appl. Climatol.* **2017**, *130*, 77–90. [CrossRef]
22. Morales, F.E.C.; Rodrigues, D.T. Spatiotemporal Nonhomogeneous Poisson Model with a Seasonal Component Applied to the Analysis of Extreme Rainfall. *J. Appl. Stat.* **2022**. [CrossRef]
23. McLeod, J.; Shepherd, M.; Konrad, C.E. Spatio-Temporal Rainfall Patterns around Atlanta, Georgia and Possible Relationships to Urban Land Cover. *Urban Clim.* **2017**, *21*, 27–42. [CrossRef]
24. Kirshen, P.; Aytur, S.; Hecht, J.; Walker, A.; Burdick, D.; Jones, S.; Fennessey, N.; Bourdeau, R.; Mather, L. Integrated Urban Water Management Applied to Adaptation to Climate Change. *Urban Clim.* **2018**, *24*, 247–263. [CrossRef]
25. Gidhagen, L.; Olsson, J.; Amorim, J.H.; Asker, C.; Belusic, D.; Carvalho, A.C.; Engardt, M.; Hundecha, Y.; Körnich, H.; Lind, P.; et al. Towards Climate Services for European Cities: Lessons Learnt from the Copernicus Project Urban SIS. *Urban Clim.* **2020**, *31*, 100549. [CrossRef]
26. Rodrigues, D.T.; Gonçalves, W.A.; Spyrides, M.H.; Andrade, L.D.; de Souza, D.O.; de Araujo, P.A.; da Silva, A.C.; e Silva, C.M. Probability of Occurrence of Extreme Precipitation Events and Natural Disasters in the City of Natal, Brazil. *Urban Clim.* **2021**, *35*, 100753. [CrossRef]
27. Bezerra, B.G.; Silva, L.L.; Santos e Silva, C.M.; de Carvalho, G.G. Changes of Precipitation Extremes Indices in São Francisco River Basin, Brazil from 1947 to 2012. *Theor. Appl. Climatol.* **2019**, *135*, 565–576. [CrossRef]

28. Marengo, J.A.; Valverde, M.C.; Obregon, G.O. Observed and Projected Changes in Rainfall Extremes in the Metropolitan Area of São Paulo. *Clim. Res.* **2013**, *57*, 61–72. [CrossRef]
29. Marengo, J.A.; Torres, R.R.; Alves, L.M. Drought in Northeast Brazil—Past, Present, and Future. *Theor. Appl. Climatol.* **2017**, *129*, 1189–1200. [CrossRef]
30. Da Silva, P.E.; Santos e Silva, C.M.; Spyrides, M.H.C.; Andrade, L.d.M.B. Precipitation and Air Temperature Extremes in the Amazon and Northeast Brazil. *Int. J. Climatol.* **2019**, *39*, 579–595. [CrossRef]
31. Araujo Palharini, R.S.; Vila, D.A.; Rodrigues, D.T.; Palharini, R.C.; Mattos, E.V.; Pedra, G.U. Assessment of Extreme Rainfall Estimates from Satellite-Based: Regional Analysis. *Remote Sens. Appl. Soc. Environ.* **2021**, *23*, 100603. [CrossRef]
32. Enfield, D.B. Relationships of Inter-American Rainfall to Tropical Atlantic and Pacific SST Variability. *Geophys. Res. Lett.* **1996**, *23*, 3305–3308. [CrossRef]
33. Seth, A.; Rauscher, S.A.; Camargo, S.J.; Qian, J.H.; Pal, J.S. RegCM3 Regional Climatologies for South America Using Reanalysis and ECHAM Global Model Driving Fields. *Clim. Dyn.* **2007**, *28*, 461–480. [CrossRef]
34. Nobre, P.; Marengo, J.A.; Cavalcanti, I.F.A.; Obregon, G.; Barros, V.; Camilloni, I.; Campos, N.; Ferreira, A.G. Seasonal-to-Decadal Predictability and Prediction of South American Climate. *J. Clim.* **2006**, *19*, 5988–6004. [CrossRef]
35. Misra, V.; Zhang, Y. The Fidelity of NCEP CFS Seasonal Hindcasts over Nordeste. *Mon. Weather Rev.* **2007**, *135*, 618–627. [CrossRef]
36. Hounsou-Gbo, G.A.; Araujo, M.; Bourlès, B.; Veleda, D.; Servain, J. Tropical Atlantic Contributions to Strong Rainfall Variability along the Northeast Brazilian Coast. *Adv. Meteorol.* **2015**, *2015*, 902084. [CrossRef]
37. Duarte, J.L.; Diaz-Quijano, F.A.; Batista, A.C.; Giatti, L.L. Climatic Variables Associated with Dengue Incidence in a City of the Western Brazilian Amazon Region. *Rev. Soc. Bras. Med. Trop.* **2019**, *52*, 1–8. [CrossRef]
38. De Oliveira, P.T.; Silva, C.M.S.E.; Lima, K.C. Linear Trend of Occurrence and Intensity of Heavy Rainfall Events on Northeast Brazil. *Atmos. Sci. Lett.* **2014**, *15*, 172–177. [CrossRef]
39. Grimm, A.M.; Tedeschi, R.G. ENSO and Extreme Rainfall Events in South America. *J. Clim.* **2009**, *22*, 1589–1609. [CrossRef]
40. Min, S.K.; Zhang, X.; Zwiers, F.W.; Hegerl, G.C. Human Contribution to More-Intense Precipitation Extremes. *Nature* **2011**, *470*, 378–381. [CrossRef] [PubMed]
41. Donat, M.G.; Lowry, A.L.; Alexander, L.V.; O'Gorman, P.A.; Maher, N. More Extreme Precipitation in the Worldâ €TM s Dry and Wet Regions. *Nat. Clim. Chang.* **2016**, *6*, 508–513. [CrossRef]
42. Huntington, T.G. Evidence for Intensification of the Global Water Cycle: Review and Synthesis. *J. Hydrol.* **2006**, *319*, 83–95. [CrossRef]
43. Trenberth, K.E. Changes in Precipitation with Climate Change. *Clim. Res.* **2011**, *47*, 123–138. [CrossRef]
44. IPCC. *Climate Change 2021 The Physical Science Basis WGI*; IPCC: Geneva, Switzerland, 2021; Volume 34, ISBN 9781009157896.
45. IPCC. *IPCC Part A: Global and Sectoral Aspects. (Contribution of Working Group II to the Fifth Assessment Report of the Intergovernmental Panel on Climate Change*; Climate Change 2014: Impacts, Adaptation, and Vulnerability; IPCC: Geneva, Switzerland, 2014; p. 1132.
46. Aumann, H.H.; Behrangi, A.; Wang, Y. Increased Frequency of Extreme Tropical Deep Convection: AIRS Observations and Climate Model Predictions. *Geophys. Res. Lett.* **2018**, *45*, 13530–13537. [CrossRef]
47. Serrano-Notivoli, R.; Beguería, S.; Saz, M.Á.; de Luis, M. Recent Trends Reveal Decreasing Intensity of Daily Precipitation in Spain. *Int. J. Climatol.* **2018**, *38*, 4211–4224. [CrossRef]
48. Santos, M.; Fonseca, A.; Fragoso, M.; Santos, J.A. Recent and Future Changes of Precipitation Extremes in Mainland Portugal. *Theor. Appl. Climatol.* **2019**, *137*, 1305–1319. [CrossRef]
49. Zeder, J.; Fischer, E.M. Observed Extreme Precipitation Trends and Scaling in Central Europe. *Weather Clim. Extrem.* **2020**, *29*, 100266. [CrossRef]
50. Zhang, M.; Chen, Y.; Shen, Y.; Li, B. Tracking Climate Change in Central Asia through Temperature and Precipitation Extremes. *J. Geogr. Sci.* **2019**, *29*, 3–28. [CrossRef]
51. Saddique, N.; Khaliq, A.; Bernhofer, C. Trends in Temperature and Precipitation Extremes in Historical (1961–1990) and Projected (2061–2090) Periods in a Data Scarce Mountain Basin, Northern Pakistan. *Stoch. Environ. Res. Risk Assess.* **2020**, *34*, 1441–1455. [CrossRef]
52. Harrison, L.; Funk, C.; Peterson, P. Identifying Changing Precipitation Extremes in Sub-Saharan Africa with Gauge and Satellite Products. *Environ. Res. Lett.* **2019**, *14*, 085007. [CrossRef]
53. Gebrechorkos, S.H.; Hülsmann, S.; Bernhofer, C. Changes in Temperature and Precipitation Extremes in Ethiopia, Kenya, and Tanzania. *Int. J. Climatol.* **2019**, *39*, 18–30. [CrossRef]
54. da Silva, R.M.; Santos, C.A.G.; da Costa Silva, J.F.C.B.; Silva, A.M.; Brasil Neto, R.M. Spatial Distribution and Estimation of Rainfall Trends and Erosivity in the Epitácio Pessoa Reservoir Catchment, Paraíba, Brazil. *Nat. Hazards* **2020**, *102*, 829–849. [CrossRef]
55. Rodrigues, D.T.; Santos e Silva, C.M.; Dos Reis, J.S.; Palharini, R.S.A.; Cabral Júnior, J.B.; da Silva, H.J.F.; Mutti, P.R.; Bezerra, B.G.; Gonçalves, W.A. Evaluation of the Integrated Multi-Satellite Retrievals for the Global Precipitation Measurement (Imerg) Product in the São Francisco Basin (Brazil). *Water* **2021**, *13*, 2714. [CrossRef]
56. Silva, J.D.S.; Cabral Júnior, J.B.; Rodrigues, D.T.; Silva, F.D.D.S. Climatology and Significant Trends in Air Temperature in Alagoas, Northeast Brazil. *Theor. Appl. Climatol.* **2023**, *151*, 1805–1824. [CrossRef]
57. Wanhe, L.; Wenxiang, C. Temporal Trends Features in Consecutive Days of Extreme Precipitation over China, 1951–2017. *Mausam* **2019**, *70*, 321–328. [CrossRef]
58. Wang, W.; Tang, H.; Li, J.; Hou, Y. Spatial-Temporal Variations of Extreme Precipitation Characteristics and Its Correlation with El Niño-Southern Oscillation during 1960–2019 in Hubei Province, China. *Atmosphere* **2022**, *13*, 1922. [CrossRef]

59. Xia, Y.; Dan, D.; Liu, H.; Zhou, H.; Wan, Z. Spatiotemporal Distribution of Precipitation over the Mongolian Plateau during 1976–2017. *Atmosphere* **2022**, *13*, 2132. [CrossRef]
60. Zechie, P.R.; Chiao, S. Climate Variability of Atmospheric Rivers and Droughts over the West Coast of the United States from 2006 to 2019. *Atmosphere* **2021**, *12*, 201. [CrossRef]
61. Brazel, A. June Temperature Trends in the Southwest Deserts of the USA (1950–2018) and Implications for Our Urban Areas. *Atmosphere* **2019**, *10*, 800. [CrossRef]
62. Dunn, R.J.H.; Alexander, L.V.; Donat, M.G.; Zhang, X.; Bador, M.; Herold, N.; Lippmann, T.; Allan, R.; Aguilar, E.; Barry, A.A.; et al. Development of an Updated Global Land In Situ-Based Data Set of Temperature and Precipitation Extremes: HadEX3. *J. Geophys. Res. Atmos.* **2020**, *125*, e2019JD032263. [CrossRef]
63. Sillmann, J.; Thorarinsdottir, T.; Keenlyside, N.; Schaller, N.; Alexander, L.V.; Hegerl, G.; Seneviratne, S.I.; Vautard, R.; Zhang, X.; Zwiers, F.W. Understanding, Modeling and Predicting Weather and Climate Extremes: Challenges and Opportunities. *Weather Clim. Extrem.* **2017**, *18*, 65–74. [CrossRef]
64. Morales, F.E.C.; Vicini, L.; Hotta, L.K.; Achcar, J.A. A Nonhomogeneous Poisson Process Geostatistical Model. *Stoch. Environ. Res. Risk Assess.* **2017**, *31*, 493–507. [CrossRef]
65. Campion, W.M.; Rubin, D.B. *Multiple Imputation for Nonresponse in Surveys*; John Wiley & Sons, Inc.: Hoboken, NJ, USA, 1989; Volume 26, ISBN 047108705X.
66. Honaker, J.; King, G.; Blackwell, M. Amelia II: A Program for Missing Data, R Package Version 1.5., 2012. *J. Stat. Softw.* **2011**, *45*, 1–3.
67. IBGE Instituto Brasileiro de Geografia e Estatística (IBGE). Estimativas Da População Residente No Brasil e Unidades Da Federação Com Data de Referência Em 1º de Julho de 2021. *Inst. Bras. Geogr. Estat.* **2021**, 1–119.
68. de Abreu, L.P.; Gonçalves, W.A.; Mattos, E.V.; Mutti, P.R.; Rodrigues, D.T.; da Silva, M.P.A. Clouds' Microphysical Properties and Their Relationship with Lightning Activity in Northeast Brazil. *Remote Sens.* **2021**, *13*, 4491. [CrossRef]
69. Calderari, E.B.; Gomes, C.P.; Beatrice, F.D.O.; Torres, R.L. As Contribuições Da Nova Sudene Para o Desenvolvimento Do Nordeste. *Rev. Grifos* **2019**, *29*, 11. [CrossRef]
70. Rao, V.B.; Franchito, S.H.; Santo, C.M.E.; Gan, M.A. An Update on the Rainfall Characteristics of Brazil: Seasonal Variations and Trends in 1979–2011. *Int. J. Climatol.* **2016**, *36*, 291–302. [CrossRef]
71. Chaves, R.R.; Cavalcanti, I.F.A. Atmospheric Circulation Features Associated with Rainfall Variability over Southern Northeast Brazil. *Mon. Weather Rev.* **2001**, *129*, 2614–2626. [CrossRef]
72. Carvalho, L.M.V.; Jones, C.; Liebmann, B. The South Atlantic Convergence Zone: Intensity, Form, Persistence, and Relationships with Intraseasonal to Interannual Activity and Extreme Rainfall. *J. Clim.* **2004**, *17*, 88–108. [CrossRef]
73. Nobre, P.; Shukla, J. Variations of Sea Surface Temperature, Wind Stress, and Rainfall over the Tropical Atlantic and South America. *J. Clim.* **1996**, *9*, 2464–2479. [CrossRef]
74. Boers, N.; Bookhagen, B.; Marwan, N.; Kurths, J.; Marengo, J. Complex Networks Identify Spatial Patterns of Extreme Rainfall Events of the South American Monsoon System. *Geophys. Res. Lett.* **2013**, *40*, 4386–4392. [CrossRef]
75. Figueroa, S.N.; Bonatti, J.P.; Kubota, P.Y.; Grell, G.A.; Morrison, H.; Barros, S.R.M.; Fernandez, J.P.R.; Ramirez, E.; Siqueira, L.; Luzia, G.; et al. The Brazilian Global Atmospheric Model (BAM): Performance for Tropical Rainfall Forecasting and Sensitivity to Convective Scheme and Horizontal Resolution. *Weather Forecast.* **2016**, *31*, 1547–1572. [CrossRef]
76. Lucena, R.L.; Borges Da Silva, F.E.; De Medeiros Aprígio, T.R.; Bezerra Cabral Júnior, J. The Influence of Altitude on the Climate of Semiarid Areas: Contributions to Conservation. *Int. J. Clim. Chang. Impacts Responses* **2022**, *14*, 81–93. [CrossRef]
77. Lyra, G.B.; Oliveira-Júnior, J.F.; Zeri, M. Cluster Analysis Applied to the Spatial and Temporal Variability of Monthly Rainfall in Alagoas State, Northeast of Brazil. *Int. J. Climatol.* **2014**, *34*, 3546–3558. [CrossRef]
78. Barbieri, A.F.; Guedes, G.R.; Noronha, K.; Queiroz, B.L.; Domingues, E.P.; Rigotti, J.I.R.; da Motta, G.P.; Chein, F.; Cortezzi, F.; Confalonieri, U.E.; et al. Population Transitions and Temperature Change in Minas Gerais, Brazil: A Multidimensional Approach. *Rev. Bras. Estud. Popul.* **2015**, *32*, 461–488. [CrossRef]
79. Macedo, M.J.H.; de Souza Guedes, R.V.; de Sousa, F.D.A.S.; da Cunha Dantas, F.R. Análise Do Índice Padronizado de Precipitação Para o Estado Da Paraíba, Brasil. *Rev. Ambient. Agua* **2014**, *9*, 445–458. [CrossRef]
80. Zanella, M.E. Análise Multitemporal Dos Desastres Naturais Hidroclimatológicos Do Estado Do Ceará: Contribuições Das Geotecnologias à Gestão Dos Riscos Naturais. *Rev. Geonorte* **2012**, *1*, 907–920.
81. Morales, F.E.C.; Vicini, L. A Non-Homogeneous Poisson Process Geostatistical Model with Spatial Deformation. *AStA Adv. Stat. Anal.* **2020**, *104*, 503–527. [CrossRef]
82. Goel, A.L. *A Guidebook for Software Reliability Assessment*; Syracuse University: Syracuse, NY, USA, 1983.
83. Sampson, P.D.; Guttorp, P. Estimation of Nonstationary Nonparametric Spatial Covariance Structure. *J. Am. Stat. Assoc.* **2014**, *87*, 108–119. [CrossRef]
84. Gomes, H.B.; Ambrizzi, T.; Pontes da Silva, B.F.; Hodges, K.; Silva Dias, P.L.; Herdies, D.L.; Silva, M.C.L.; Gomes, H.B. Climatology of Easterly Wave Disturbances over the Tropical South Atlantic. *Clim. Dyn.* **2019**, *53*, 1393–1411. [CrossRef]
85. Kousky, V.E. Frontal Influences on Northeast Brazil. *Mon. Weather Rev.* **1979**, *107*, 1140–1153. [CrossRef]
86. Zhou, J.; Lau, K.M. Principal Modes of Interannual and Decadal Variability of Summer Rainfall over South America. *Int. J. Climatol.* **2001**, *21*, 1623–1644. [CrossRef]

87. Reboita, M.S.; Rodrigues, M.; Silva, L.F.; Alves, M.A. Aspectos Climáticos Do Estado de Minas Gerais. *Rev. Bras. Climatol.* **2015**, *17*, 206–226.
88. Palharini, R.S.A.; Vila, D.A.; Rodrigues, D.T.; Quispe, D.P.; Palharini, R.C.; de Siqueira, R.A.; de Sousa Afonso, J.M. Assessment of the Extreme Precipitation by Satellite Estimates over South America. *Remote Sens.* **2020**, *12*, 2085. [CrossRef]
89. Araújo Palharini, R.S.; Vila, D.A. Climatological Behavior of Precipitating Clouds in the Northeast Region of Brazil. *Adv. Meteorol.* **2017**, *2017*, 5916150. [CrossRef]
90. Reis, L.; Silva, C.M.S.E.; Bezerra, B.; Mutti, P.; Spyrides, M.H.; Silva, P.; Magalhães, T.; Ferreira, R.; Rodrigues, D.; Andrade, L. Influence of Climate Variability on Soybean Yield in Matopiba, Brazil. *Atmosphere* **2020**, *11*, 1130. [CrossRef]